Thermal stability, phase transformations and mechanical properties of a Fe64B24Y4Nb6 metallic glass

Marie-Noëlle Avettand-Fènoël, Maya Marinova, Roland Taillard, Wei Jiang

Thermal stability, phase transformations and mechanical properties of a $Fe_{64}B_{24}Y_4Nb_6$ metallic glass.

M.-N. Avettand-Fènoël [a*], M. Marinova [b], R. Taillard [a], Wei Jang [c]

a: Univ. Lille, CNRS, INRAE, Centrale Lille, UMR 8207 – UMET - Unité Matériaux Et Transformations, F-59000 Lille, France

b: Univ. Lille, CNRS, INRA, Centrale Lille, Univ. Artois, FR 2638 – IMEC – Institut Michel-Eugène Chevreul, F-59000 Lille, France

c: School of Materials Science and Engineering, Hefei University of Technology, Hefei 230009, China

* Corresponding author – E-mail: marie-noelle.avettand-fenoel@univ-lille.fr
Tel: 33(0)320436927

Abstract

$Fe_{64}B_{24}Y_4Nb_6$ metallic glass ribbon and its bulk counterpart were characterized by conventional and high rate differential scanning calorimetry, electron probe microanalysis, in-situ X-ray diffractometry, high resolution transmission electron microscopy and instrumented microhardness. The metallic glass possesses a high glass forming ability. It is thermally stable up to 585~~596~~°C while primary crystallization of Fe_2B and FeB occurs at 677°C. Estimated by the Kissinger and Moynihan's methods, the activation energy of glass transition was shown to be lower than that of primary crystallization. After total crystallization, the bulk alloy contains a terminal Fe solid solution, Fe_2B, FeB, $Fe_3B_8Nb_7$ and $BFe_{14}Y_2$ phases while the ribbon contains additional yttria as well. The loading and unloading curves as well as the indentation features are very suitable in order to evidence the effect of the various crystallization events on the mechanical behavior of the bulk alloy. The hardness of the amorphous and fully crystallized bulk alloys amount to 1198±21 and 461±65 $HV_{0.5}$, respectively and their reduced Young modulus are close to 174±5 GPa. The deformation ability of the fully crystallized alloy is twice that of the glassy alloy.

Keywords

Metallic glass; thermal stability; crystallization; microstructure; instrumented microhardness

1. Introduction

The class of the metallic glasses (MG) is very widespread and among them, the Fe based metallic glasses are particularly attractive for various applications such as sensors, inductor cores or radio-frequency identification systems because of their soft magnetic properties with rather high saturation magnetization, their high electrical resistivity, their elevated mechanical strength and their low cost **[1-2]**. The early Fe based metallic glasses (Fe-P-C) ribbons have been developed in 1967 and since then, many other Fe-based MG with distinct chemical compositions were designed as reported in different reviews **[1-2]**.

The design of bulk multicomponent metallic glasses is rendered possible provided the three following empirical rules proposed by Inoue are checked. The materials should contain more than 3 elements, with a significant difference in atomic size, namely above 12% among the main three elements. There should be negative heats of mixing among their elements **[1-4]**. This leads to an increase of the degree of randomly dense packed structure on the

topological and chemical points of view, hence to the formation of a liquid with multicomponent short-range interactions. This order entails i) an increase of the solid/liquid interfacial energy leading to the suppression of crystalline phase nucleation, ii) a reduction of the atomic diffusivity and an augmentation of viscosity originating atomic rearrangement hindering and glass transition temperature rise and iii) the necessity of long-range atomic rearrangement for crystallization to occur and thus suppression of crystalline phase growth **[3]**. In addition, according to Lin, the production of a FeBM metallic glass (M for metal) requires that (i) M is an element with an atomic radius at least 130% that of Fe, (ii) M generates eutectics with both Fe and B and (iii) the M-Fe eutectic is at the Fe-rich end of the binary equilibrium phase diagram **[5]**.

A $Fe_{64}B_{24}Y_4Nb_6$ metallic glass has been developed for the present study on the background of literature papers dealing with other Fe-B-Y-Nb metallic glasses which all present a high glass forming ability and a large supercooled liquid region **[6-12]**. The latter material state can be relevant during metal forming. For the designed $Fe_{64}B_{24}Y_4Nb_6$, the aforementioned requirements exposed by Inoue to obtain a metallic glass are met since

(i) Fe, B, Y and Nb atoms present Goldschmidt radii of 128 pm, 97 pm, 181 pm and 147 pm, respectively **[13]**, which satisfies the condition related to the difference in atomic size;

(ii) the heats of mixing are -50 to -35 kJ/mol, -26 to -16 kJ/mol, -39 kJ/mol and -16 kJ/mol for the Y-B, Fe-B, Nb-B and Fe-Nb systems, respectively, **[2,8,12,14]** while that for Y-Nb is positive (30 kJ/mol) **[11,15]** and

(iii) Fe-B and Fe-Nb present a deep eutectic **[13]**.

Y was added since it was expected to trap oxygen. Y indeed presents an O scavenging role since the -1904 kJ/mol Gibbs energy of Y_2O_3 formation is very low compared to the -820.5 kJ/mol, -1273 kJ/mol and -101 kJ/mol values for Fe_2O_3, B_2O_3 and Nb_2O_5, respectively **[12,13].**

The aims of the present study consist in analyzing the thermal stability at conventional and high heating rates of the present $Fe_{64}B_{24}Y_4Nb_6$ metallic glass ribbon and of its bulk counterpart and characterizing their phase transformations as well as some of their mechanical properties.

2. Experimental procedure

The $Fe_{64}B_{24}Y_4Nb_6$ master alloy was produced, from high purity metallic elements, by arc melting under a high purity argon atmosphere, after the melting of titanium, set next to the crucible containing the master alloy, for residual oxygen removal. The alloy was re-melted four times to ensure its chemical homogeneity. Quenched alloys with the $Fe_{64}B_{24}Y_4Nb_6$ composition were then elaborated as melt spun ribbons or as bulk rods. The 2 mm wide, 50 µm thick and 30 mm long ribbons were prepared by single-roller melt spinning on a Cu rotating wheel ~~at a cooling speed of 10^5 °C/s. Besides,~~while the 2 mm diameter bulk rods were obtained ~~at a cooling speed of 550°C/s~~ by injection of the molten alloys in a water-cooled copper mold.

Table 1 summarizes the measured chemical composition of the metallic glass. The C, N and O contents were measured by LECO, while the B, Nb and Y amounts were evaluated by Inductively Coupled Plasma (ICP) – Atomic Emission Spectrometry (AES) after mineralization of the samples. The Fe content was finally estimated by difference. According to table 1, the metallic glass is Al bearing, Al very likely coming from impurities left on the wall of arc melting furnace chamber.

Table 1: Chemical composition of the bulk metallic glass (at.%).

Element	Fe	B	Nb	Y	C	Bi	Cr
at.%	64.305477 ±0.000090.009	24.6005977 ±0.000500.050	6.037668 ±0.000050.005	4.346562 ±0.000060.006	0.113268 ±0.000420.042	0.00208 ±0.000020.002	0.01021 ±0.000090.009
Cu	**Mn**	**Al**	**Pb**	**Si**	**As**	**N**	**O**
0.03346 ±0.000080.008	0.031079 ±0.000090.009	0.42927 ±0.000180.018	0.077691 ±0.000020.002	0.01527 ±0.000080.008	0.00451 ±0.000070.007	<0.000360.036	<0.000310.031

The thermal stability of the quenched alloys was investigated through conventional and high-rate differential scanning calorimetry (DSC) analyses. The conventional DSC analyses were performed in alumina pans under flowing argon using a DSC404C Netzsch™ equipment at heating rates in-between 10 and 50 K/min and temperatures from room temperature up to 1400°C. For high-rate DSC, a Mettler Toledo Flash DSC2™ calorimeter with chip sensors was used. The experiments were achieved from room temperature up to 1000°C under flowing argon so as to investigate the effect of the 500, 1000 and 5000 K/s high heating rates on the metallic alloys phase transformations. Owing to the absence of melting of the $Fe_{64}B_{24}Y_4Nb_6$ alloys below the 1000°C maximum temperature allowed by the flash DSC equipment, the sample was changed at each run in order to analyze the effect of a single thermal cycle on the phase transformations of the raw metallic glass.

In conventional differential scanning calorimetry, some interrupted thermal treatments were achieved at a heating rate of 10 K/min and a cooling rate of 50 K/min in order to identify the phase transformations generating the endo or exothermal peaks detected in the DSC patterns.

The samples were grinded and polished up to the 1 µm grade. Their microstructure was analyzed by means of a Cameca SX 100™ electron probe microanalyzer (EPMA) equipped with an X-ray wavelength dispersive spectrometer (WDS). The boron content was calculated by difference with the total amount of the Fe, Nb, O and Y remaining elements. Nevertheless, as the B content measurement is very ticklish and dependent on the B bearing crystal structures **[16]**, the presented X-ray maps only enable to differentiate the phases according to their qualitative chemical composition.

Besides, some thin foils of the ribbon in the metallic glass quenched state or at the beginning of first crystallization were prepared by focused ionic beam (FIB) with a FEI Strata DB 235 ™ device. They were then analyzed by transmission electron microscopy using a FEI Titan Themis 300 ™ microscope, equipped with a probe aberration corrector and a monochromator, allowing spatial resolution of 70 pm and energy resolution of 150 meV. The microscope has also a super-X windowless 4 quadrant SDD (silicon drift detector) detection system for the STEM-EDX (Scanning Transmission Electron Microscopy - Energy Dispersive Spectroscopy) mapping and several annual dark field detectors. The experiment has been performed at 300 kV with a spot size of about 500 pm, semi-convergence angle of 21 mrad and probe current of approximately 100 pA. For the high angle annular dark field (HAADF) images, collection angles have been between 50 mrad and 200 mrad.

In situ X-ray microdiffraction was performed on a 140 µm diameter area of the ribbon set on a silicon support in a Rigaku™ equipment. These analyses were executed at a heating rate of 10 K/min under He and with a Cu anticathod (λ=1.54060 Å). The diffractograms were registered every 25°C over the 25 to 900°C temperature range. X-ray microdiffraction was also performed on a 140 µm diameter area of the bulk sample after interrupted heat

treatments. The latter experiments were performed under air at room temperature and again with a silicon support and a Cu anticathod (λ=1.54060 Å).

Instrumented Vickers hardness tests were finally carried out under 500 g with a MHT CSM Instruments^{TR} device to estimate both the hardness, the Young modulus and the rigidity of the bulk alloy either in the quenched state or after heat treatments. Four tests were performed by sample.

3. Results

3.1. Raw samples

The observation of the ribbons reveals that one face is shiny while the other one is dull. This suggests that there was a thermal gradient during the elaboration of the ribbon and that there were different solidification rates on both faces of the ribbon. The difference of shininess may also result from the process for which the ribbon face in close contact with the wheel presents a dull aspect. According to the X-ray diffraction analyses, both sides of the ribbon are rather amorphous as evidenced by the broad hump proving the absence of long-range order. A small X-ray diffraction peak may however exist on the pattern of the shiny face (figure 1). This peak very likely results from the temperature gradient across the ribbon thickness which causes a difference of solidification rate between both ribbon faces. The existence of a critical solidification rate is indeed evidenced by this trend towards partial crystallization which is more pronounced on the ribbon face in direct contact with the atmosphere which presents the smaller cooling rate **[17]** (figure 1). Contrary to numerous literature data, the present observation proves that the melt spun ribbon face with the more intense metallic luster is not always the face with the more amorphous structure.

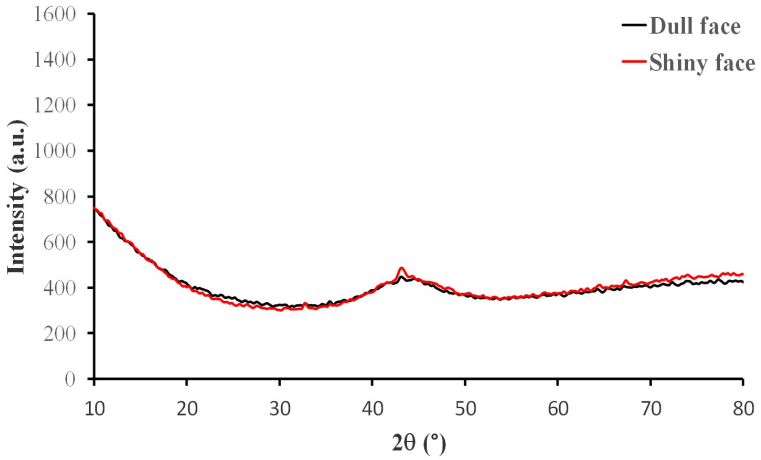

Figure 1: Room temperature X-ray diffraction patterns of the shiny and dull faces of the ribbon at the quenched state.

In addition, figure 2 displays a TEM image of the ribbon at the quenched state. The selected area electron diffraction pattern (SAEDP) presents two diffuse and continuous rings corresponding to the 0.205 and 0.124 nm mean atoms spacings. These rings unveal the existence of organized domains within an amorphous matrix. Two of these ordered zones with interatomic spacings corresponding to the aforementioned distances are for instance encircled in figure 2.

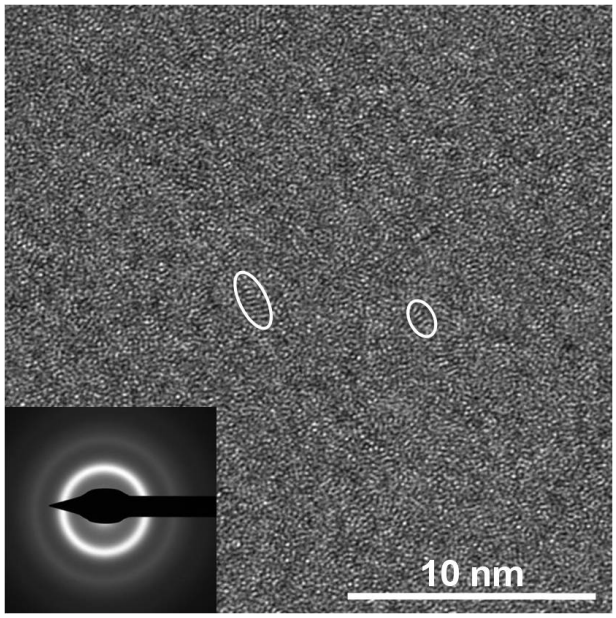

Figure 2: TEM image of the quenched alloy ribbon and the corresponding SAEDP.

Besides, figure 3 shows important microstructural features inside one of the bulk rods at the quenched state. Concentric segregation zones decorated by submicrometric crystals are detected in the back scattered electrons (BSE) mode. These B and Nb bearing crystals contain less Fe and Y than the matrix. This means that for this particular rod, the cooling rate was not sufficient and lower than the critical cooling rate required to avoid primary crystallization during the elaboration process.

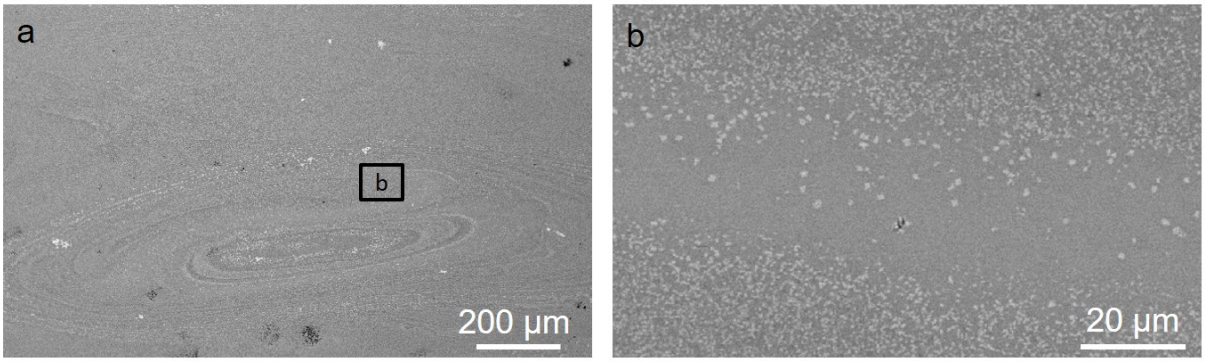

Figure 3: Microstructure within a bulk sample at the raw state (EPMA/BSE).

3.2. Thermal stability of the metallic glasses?

According to the DSC patterns depicted in figure 4, both metallic glasses, ribbon shaped and bulk, present the same behavior during the 10 K/min heating stage. Upon heating, after a Tg glass transition endothermic peak, they present a supercooled liquid region followed by four exothermal crystallizations (Tx_i, i = 1 to 4) and at last by an important endothermal peak. The onset temperature of the latter transformation corresponds to the melting temperature, i.e. to the beginning of melting, while its offset temperature stands for the liquidus temperature. For the ribbon, an additional endothermal peak (Tx_5) was also detected between Tx_4 and the melting event. The onset temperatures of the common reactions are very close for both kinds of metallic glass (table 2). The high ratio between (Tx_1-Tg) and (T liquidus-Tg) suggests their high thermoplastic formability (table 2); Many

studies reported in literature have indeed already shed light on the high formability of supercooled metallic glasses of different natures **[18-21]**.

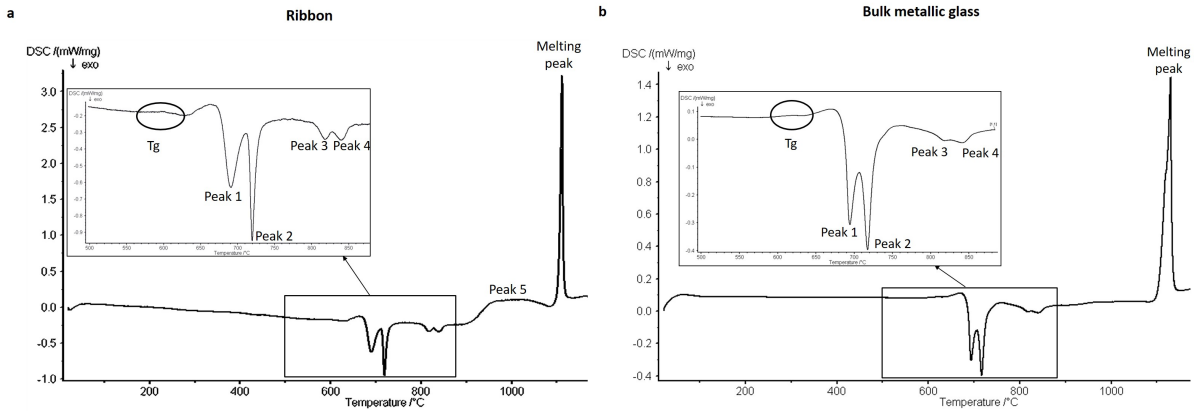

Figure 4: DSC pattern of the metallic glass at a heating rate of 10 K/min. The sample mass was 6.710 mg for the ribbon (a) and 74.719 mg for the bulk (b) sample, respectively. The inserts in the figure are local enlargements of the curves evidencing the glass transition.

Table 2: Data from the DSC patterns recorded at a heating rate of 10 K/min (temperatures in K). Tg stands for the glass transition temperature measured at the onset of the transformation, Tx_i (i = 1 to 5) for the onset temperature of the *i* crystallization ~~peak onset temperature~~ event. Because of the convolution of peaks 1 and 2 and peaks 3 and 4, the determination of the peaks 2 and 4 onset temperature is somewhat inaccurate. The melting temperature and liquidus temperature are assumed to be the onset and end temperatures of the prominent endothermic peak.

Sample	Tg	Tx_1	Tx_2	Tx_3	Tx_4	Tx_5	Tx_1-Tg=ΔT	Melting temperature	T liquidus	Tg/T liquidus (reduced glass transition)	ΔT/(Tliquidus-Tg)
Ribbon	~~868.7~~858.0	950.6	988.7	1080.2	Difficult to estimate	1184.1	~~81.9~~92.6	1379.1	1397.2	0.62	~~0.155~~0.172
Bulk	865.7	960.8	984.2	1076.4	Difficult to estimate	-	95.1	1391.8	1421.9	0.61	0.171

As expected, and according to the DSC analyses, the phase transformations are delayed with an increase of the heating rate as exemplified in figure 5.

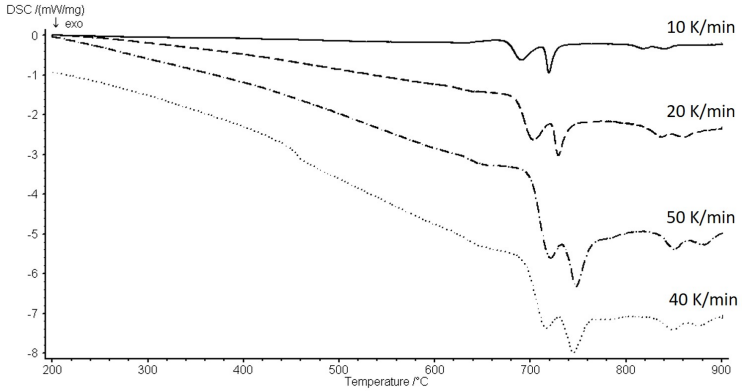

Figure 5: Effect of heating rate on the metallic glass ribbon phase transformations (the sample mass was 6.710, 2.964, 2.730 and 2.801 mg for the 10, 20, 40 and 50°C/min heating rate, respectively).

In order to determine the apparent activation energy of both the glass transition and primary crystallization, the Kissinger's analysis **[22,23]** was performed based on equation 1

$$\ln\left(\frac{\beta}{T^2}\right) = -\frac{E}{RT} + C \qquad (1)$$

where β is the heating rate, T is either the peak temperature of the primary crystallization or of the ~~Tg~~ glass transition ~~temperature~~, E is the apparent activation energy, R is the perfect gas constant and C is a constant. The slope of the plot of $\ln(\beta/T^2)$ *vs.* 1/T presented in figures 6a and b is used to calculate the apparent activation energy of the glass transition and of the primary crystallization for the ribbon. They amount to ~~1.2874×10^5 J/mol~~305.7 kJ/mol and ~~4.0080×10^5 J/mol~~ 400.80 kJ/mol, respectively, by considering the 10, 20, 40 and 50 K/min lower heating rates (figure 6a). If the high heating rates of 500, 1000 and 5000 K/s are also considered, these activation energies increase to ~~3.59434×10^5 J/mol~~438.3 kJ/mol and ~~7.32674×10^5 J/mol~~ 732.67 kJ/mol, respectively (figure 6b).

Owing to its usual application to ~~phases changes~~glass transition in amorphous materials, the Moynihan's method **[24-25]** was also considered to evaluate the apparent activation energy of ~~the phase transformations~~glass transition. This approach relies on equation 2:

$$d(\ln\beta) / d(1/T) = -E/R \qquad (2)$$

According to this relation, the slope of the plot of ln(β) *vs.* 1/(RT) presented in figures 6c and d gives the apparent activation energy of the glass transition ~~and of the primary crystallization~~ for the ribbon. ~~They~~It amounts to ~~1.4313×10^5 J/mol~~ 320.4 kJ/mol~~and 4.1709×10^5 J/mol, respectively,~~ by considering the 10, 20, 40 and 50 K/min lower heating rates (figure 6c). If the high heating rates of 500, 1000 and 5000 K/s are also considered, ~~these~~this apparent activation energ~~ies~~y increases to ~~3.7502×10^5 J/mol~~ 454.2 kJ/mol~~and 7.4983×10^5 J/mol, respectively~~ (figure 6d). It is worth noting that the results are very close to those obtained with the Kissinger's equation.

According to these results, the nucleation of primary crystals requires a larger activation energy than glass transition, as it implies important changes of the atomic arrangement even within the short range ordered domains depicted in figure 2. Primary crystallization indeed requires at least a perfecting of the crystal lattice. In addition, the existence of two values of the activation energy according to the heating rate, proves that both phase transformations are hampered at high heating rates. This may suggest a control of crystallization by nucleation.

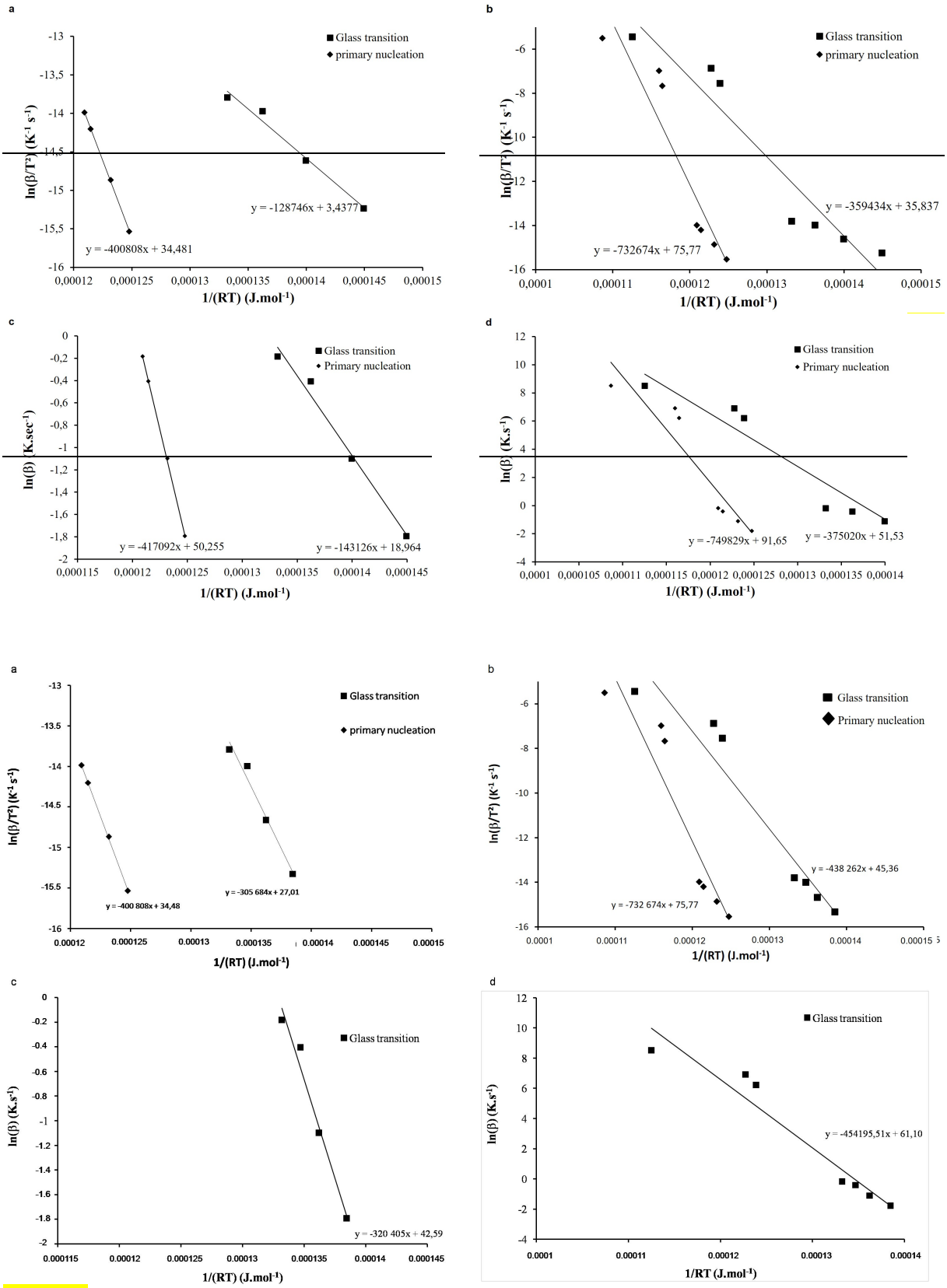

Figure 6: Kissinger analysis for the ribbon by considering the 10 K/min, 20 K/min, 40 K/min and 50 K/min (a) plus the 500, 1000 and 5000 K/s (b) heating rates. The lines are the linear fits for $\ln(\beta/T^2)$ *vs.* 1/RT, where T is either the glass transition peak temperature or the peak temperature ~~at peak maximum~~ of the primary crystallization.

Moynihan's method for the ribbon by considering the 10 K/min, 20 K/min, 40 K/min and 50 K/min (c) plus the 500, 1000 and 5000 K/s (d) heating rates. The lines are the linear fits for ln(β) *vs*. 1/T, where T is ~~either~~ the glass transition temperature at the peak maximum ~~or the maximum peak temperature of the primary crystallization~~.

The fragility index *m* defined as the rate of viscosity increase of an undercooled liquid at the glass transition temperature in the cooling process **[~~24~~26]** is given by equation 3:

$$m = E/(R \times T \times \ln 10) \quad (3)$$

with E, the apparent activation energy.

This index enables to classify the glass forming liquid either as strong or fragile liquid when *m* is below 16 or in-between 16 and 200, respectively **[~~24~~25]**. According to **[2]**, strong liquids are on the contrary qualified by m values under 20 to 40, and fragile liquids by m values in-between 60 and 150 **[~~24~~25]**. According to the first classification **[25]**, t~~T~~he present metallic glass, whose m value ~~remains below 16~~ is close to 26-27 with a heating rate of 10 K/min, is then a ~~strong~~ fragile liquid irrespective of the method employed to determine the activation energy of the glass transition (table 3).

Table 3: Apparent activation energy for both the glass transition and primary crystallization of the ribbon at a heating rate of 10 K/min. The fragility index has been estimated using the Kissinger's and the Moynihan's methods. Glass transition temperature was measured here at the peak maximum.

	Heating rate (K/min)	T (K)	Activation energy deduced from Kissinger's method (kJ/mol)	Activation energy deduced from Moynihan's method (kJ/mol)	Fragility index m by Kissinger's method	Fragility index m by Moynihan's method
Glass transition	10	868.7	~~128.74~~ 438.3	~~143.13~~ 454.2	~~7.74~~ 26.3	~~8.60~~ 27.3
Primary crystallization	10	964.1	400.80	~~417.09~~	-	-

3.3. Phase transformations

3.3.1. Primary crystallization

According to the DSC analyses (figure 4 and table 2), the primary crystallization peak occurs at 677.6°C with the ribbon. In order to identify the nature of the primary crystal, the metallic glass ribbon was heated at 10 K/min up to the 681°C very slightly higher temperature and cooled at 50 K/min by using the conventional DSC equipment. At the HRTEM scale, the ribbon presents some few micrometer polyhedral grains (zone 1), with a heterogeneous distribution and a low surface fraction, and smaller 150 nm sized spheroidal particles (zone 2) dispersed inside a metallic glass matrix (zone 3) (figure 7).

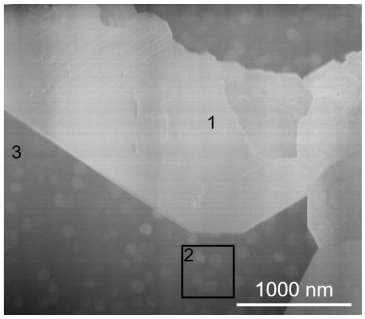

Figure 7: Microstructure of the ribbon heated up to 681°C with the 10 K/min heating rate (HAADF image).

The electron diffraction analysis of zone 1 revealed that it consists of large $Fe_3Nb_7B_8$ particles (figure 8), very likely formed during the quenching step of elaboration since the production process of the master alloy was a priori suitable to lead to a homogenized alloy (*see §2. Experimental procedure*). The atomic structure of zone 1 (figure 8a) indeed agrees with the structural representation of the crystalline lattice of $Fe_3Nb_7B_8$ (figure 8b) (the elements at higher atomic number are seen with the highest intensity (figure 8a)) and the electron diffraction pattern of zone 1 (figure 8c) is consistent with Vesta simulation of $Fe_3Nb_7B_8$ structure (figure 8d). It is however worth noting that light elements such as boron present in a crystalline network of heavy atoms cannot be seen in the HAADF micrograph. Discovered by Zheng **[16]**, the $Fe_3Nb_7B_8$ phase presents a Kagome type of atoms arrangement made of a planar hexagonal lattice of Fe atoms which contains a planar hexagonal Nb lattice again containing a planar hexagonal boron lattice with a Nb atom at its centre surrounded by B atoms (figure 8b). $Fe_3Nb_7B_8$ possesses a hexagonal crystal lattice with the space group P6/mmm, and the a = 8.33460 Å and c = 3.29410 Å lattice parameters. It also contains some crystal defects such as twins and dislocations (Figure 9a) and zones of atomic disorder (encircled in figures 8a and 9b).

The rather spheroidal dendrites with a size up to 150 nm (in zone 2) (figures 7 and 10a) and a close to 50 nm spacing are the first crystals to form during heating. The EDX (not shown here) and EELS analyses (figure 11) unveil that they are enriched with Fe compared to the amorphous matrix. The electron diffraction pattern displayed in figure 10b is constituted of the diffuse rings of the metallic glass matrix and of some spots characteristic of the crystallized particles. These spots put into evidence the existence of interreticular distances of 0.25, 0.183, 0.162, 0.161, 0.160 and 0.141 nm. These distances can be ascribed to the Fe_2B compound, namely 0.253 nm [(200) Bragg peak], 0.182 nm [(112) Bragg peak], 0.162 nm [(202) Bragg peak], 0.161 nm [(310) Bragg peak] and to the FeB compound, namely 0.259 nm [(011) Bragg peak], 0.180 nm [(121) Bragg peak], 0.163 nm [(200) Bragg peak], 0.1597 nm [(211) Bragg peak], 0.142 nm [(221) Bragg peak] [~~25~~27].

According to the EELS analysis of the amorphous matrix (zone 3) (not detailed here), the Fe/Nb, Fe/Y and Nb/Y atomic ratios are equal to 3.92, 9 and 2.94, respectively, which suggests the $Fe_{36}B_xY_4Nb_{11.8}$ chemical composition, boron being not measured in the sample because B-K and Nb-$M_{5,4}$ core-loss edges are very close in energy, 188 eV and 205 eV, respectively. The latter composition can be compared with the $Fe_{64}B_{24}Y_4Nb_6$ composition of the elemental ribbon, which suggests that a great amount of Fe has been consumed to form both the micrometric (zone 1) and nanocrystalline (zone 2) particles. The Nb content has however increased despite its consumption for the formation of the particles in zone 1, which confirms that its evaluation by EELS is ticklish, because of the proximity of its peak with that of B, and thereby inaccurate.

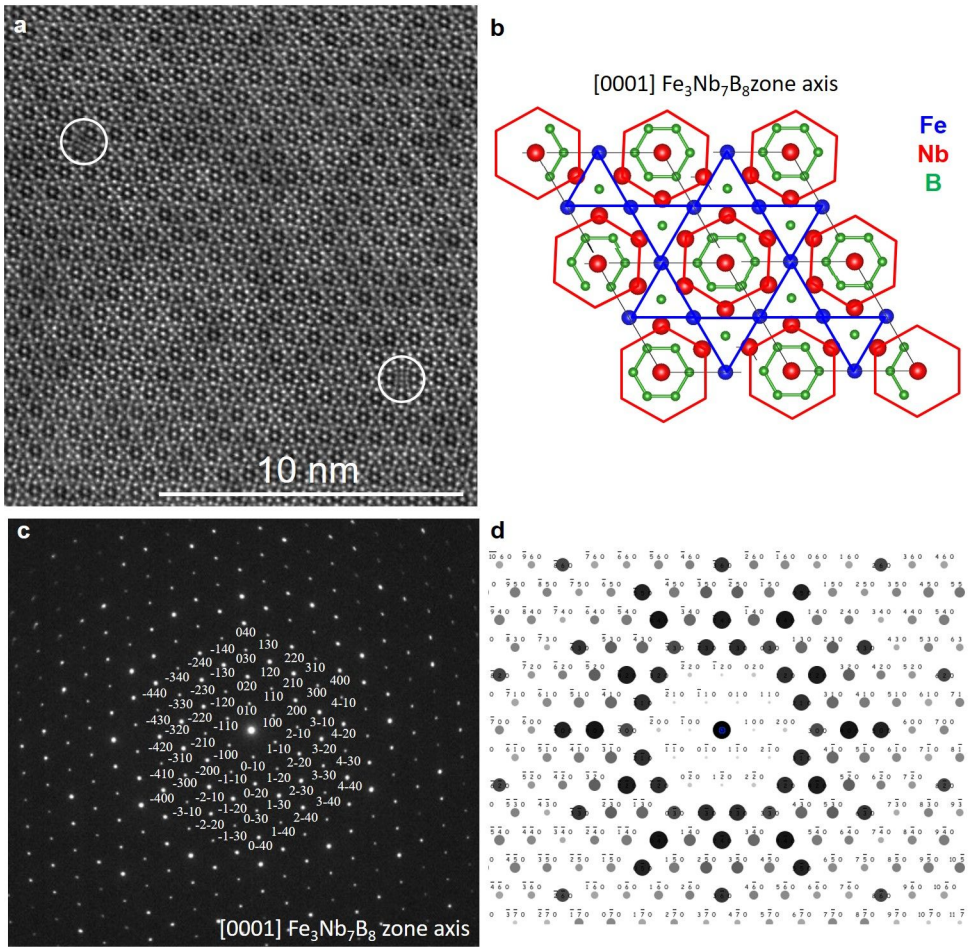

Figure 8: $Fe_3Nb_7B_8$ crystal structure of zone 1 in figure 7: atomic stacking in the (0001) planes: HAADF (a); schematics of the atomic positions in the present orientation (b); experimental electron diffraction pattern (c) and its simulation (d) along the [0001] zone axis.

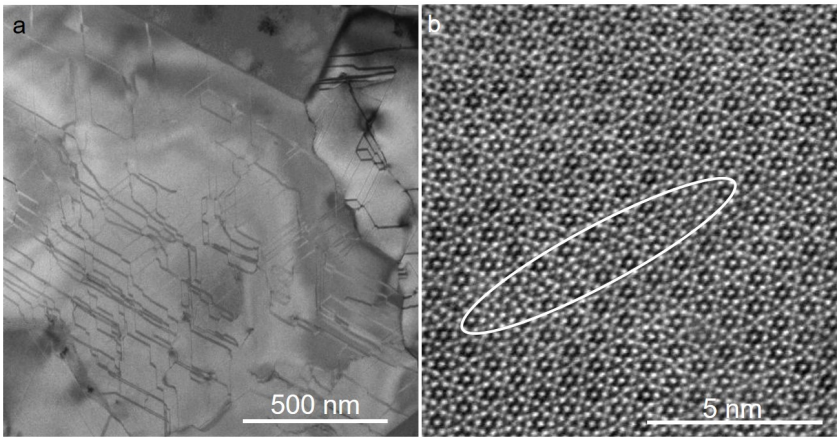

Figure 9: Defects in $Fe_3Nb_7B_8$ crystal (zone 1 in figure 7): dislocations and twins (HRTEM) (a) and atomic disorder (HAADF) (b).

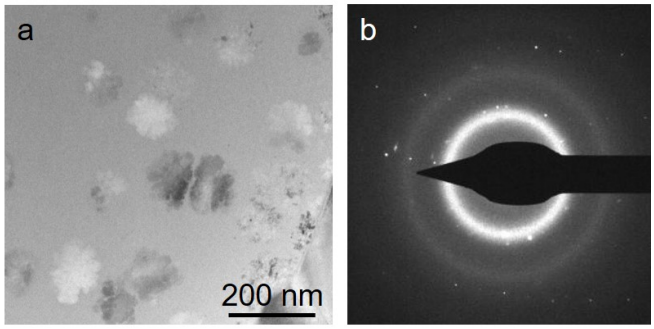

Figure 10: 150 nm sized particles (of zone 2 in figure 7) inside the matrix: (a) TEM image and (b) associated selected area electron diffraction pattern.

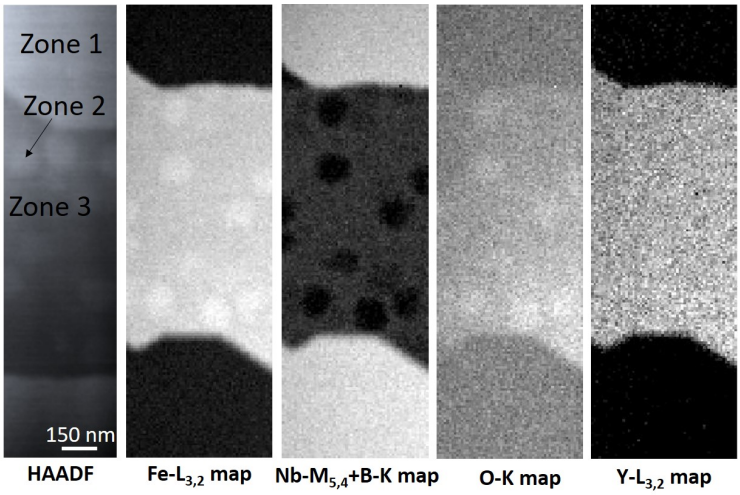

Figure 11: HAADF and EELS intensity maps of the Fe-$L_{3,2}$ (708 eV), Nb-$M_{5,4}$ (205 eV) and B-K (188 eV), O-K (530 eV) and Y-$L_{3,2}$ (2080 eV) edges for the zones 1, 2 and 3.

3.3.2. Crystallization of the metallic glass

3.3.2.1. Microstructural aspect and chemical composition of the phases.

The EPMA analyses of both the ribbons and the bulk sample after the DSC treatment up to 1400°C (figures 12 and 13) put into evidence the formation of different phases with distinct morphologies and sizes. It is worth noting that the B content measurement is quite ticklish so the quantitative contents of B are inaccurate in the X-ray maps in figures 12 and 13 in spite of the presence of the color bar. Then, as aforesaid in the *§2. Experimental procedure*, the X-ray maps just provide an idea of the phases enrichment and of the concentration ratios of the various elements except in B. Complementary XRD analyses are in fact required to identify the nature of the phases and their temperature range of formation, as shown in the following.

As depicted in the BSE micrographs in figures 12 and 13, the fully crystallized ribbon contains (i) an Fe and B bearing matrix with a grey color [phase a], (ii) some polyhedral bright particles made of B, Fe and Nb with a Fe/Nb atomic ratio close to 0.45 [phase b], (iii) an yttria phase with a light grey contrast at the ribbon borders, (iv) a eutectic constituent composed of the grey matrix [phase a] and of a dark grey phase [phase c] containing also Fe and B, but with a greater B amount than [phase a] and (v) another eutectic constituent

comprising again [phase a] and a filamentary white phase [phase d] which contains B, and equal atomic contents of Fe and Nb (figure 12).

After total crystallization, the bulk sample contains again (i) [phase a], (ii) [phase b], (iii) [phase c], (iv) a eutectic constituent between [phase a] and [phase c], (v) a eutectic between [phase a] and [phase c] and (vi) a very local eutectic constituent of [phase a] and [phase d]. It also contains large acicular particles [phase e] made of B, Fe and Y with a Fe/Y atomic ratio close to 3.7 (figure 13).

It can be noted that the formation of yttria in the ribbon instead of the Fe, Y and B bearing phase [phase e] detected in the bulk sample can very likely be explained by a distinct repartition of the elements in both metallic glasses and by the slight oxidation of the fine ribbon during the DSC analysis as Y_2O_3 was not found at the quenched state.

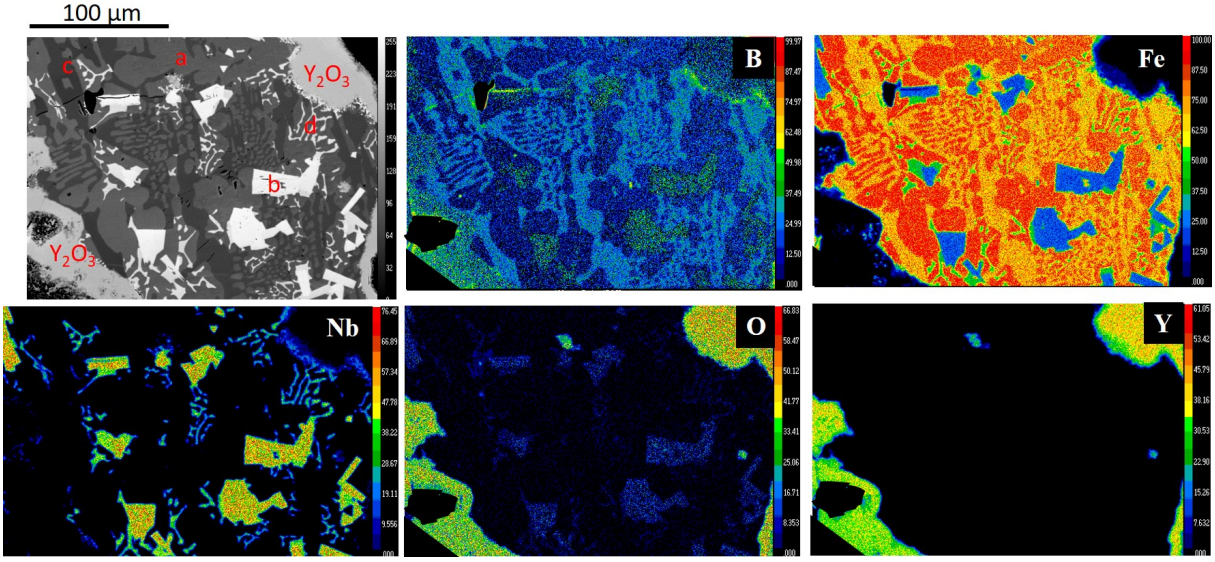

Figure 12: BSE/SEM micrograph of the ribbon after the DSC treatment up to 1400°C at the 10K/mn heating rate and associated B Kα, Fe Kα, Nb Kα, Y Kα and O Kα X-ray maps (WDS, EPMA). The color bar indicates the element content in at.%.

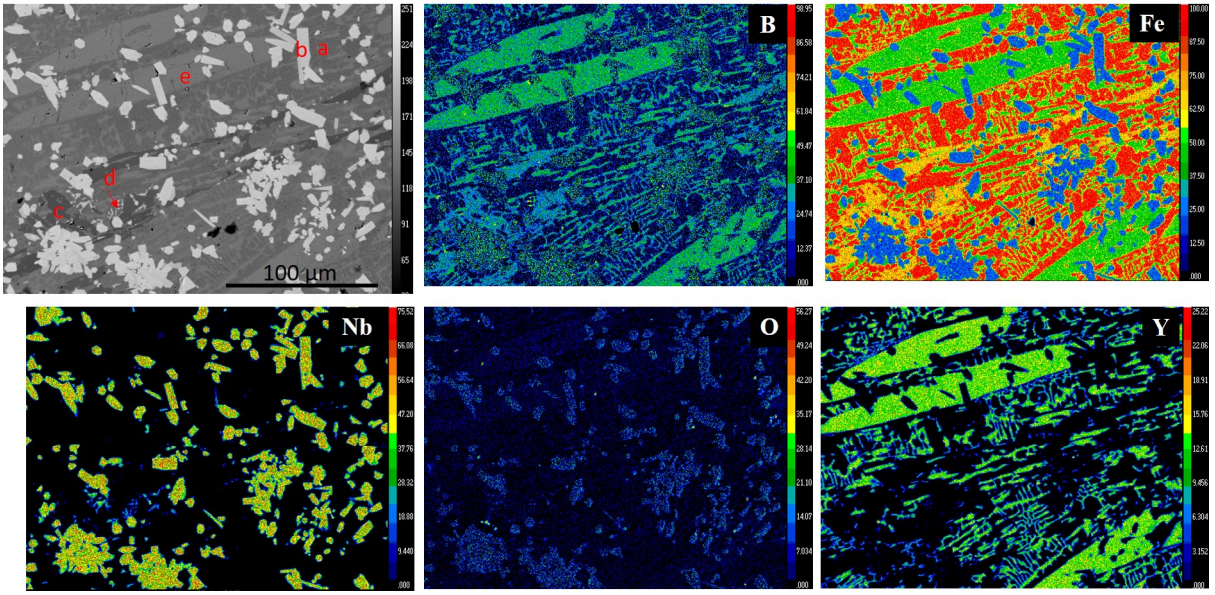

Figure 13: BSE/SEM micrograph of the bulk metallic glass after the DSC treatment up to 1400°C at the 10K/mn heating rate and associated B Kα, Fe Kα, Nb Kα, Y Kα and O Kα X-ray maps (WDS, EPMA). The color bar represents the element content in at.%.

3.3.2.2. **Phases: nature and formation temperature range.**

The in-situ X-ray diffraction patterns of the ribbon recorded *vs.* temperature (figure 14) are in agreement with the DSC analyses (figure 5) with regard to the phase transformations temperatures despite the change of the atmosphere (Ar in DSC *vs.* He in XRD and the greater thermal conductivity of He compared to Ar). Indeed, the glass transition occurs between 575°C and 600°C vs. 595.7°C in DSC. Bragg peaks then appear from 625°C against the close to 677°C temperature of primary crystallization onset determined by DSC. The identification of the various Bragg peaks exemplified here in figure 15 at 675 and 825°C remains ticklish but seems to unveil the presence of an Fe terminal solid solution [phase a], $Fe_3Nb_7B_8$ [phase b] and Fe_2B [phase c]. The existence of [phase b] has been proved by electron diffraction and it is also consistent with its close to 0.45 Fe/Nb atomic ratio measured by WDS. The existence of [phase c] has also already been evidenced by electron diffraction (see round particles in zone 2 in figure 10b). Suspected by XRD at 675°C and 825°C (figure 15), the FeB presence was confirmed by electron diffraction at 681°C (figure 10b). FeB was then also assimilated to [phase c]. $BFe_{14}Y_2$ is also suspected to exist at 825°C according to the XRD analyses (figure 15) but it was not identified by EPMA (figure 12).

X-ray diffratometry analyses of the bulk metallic glass after interrupted thermal treatments were performed at room temperature (figure 16). These heat treatments were monitored up to the onset temperatures of the four crystallization peaks, i.e. up to 690, 720, 805 and 850°C, in conventional DSC equipment with a heating rate of 10 K/min and a cooling rate of 50 K/min. A sample heated up to 1400°C at 10 K/min but slowly cooled at 10 K/min was also considered. Contrary to the latter sample case, the X-ray diffractograms of the interrupted heat treated samples exhibit the large domain of diffraction of the amorphous phase and Bragg peaks over this hump. The hump intensity decreases with the peak temperature. The analyses of the 690 and 720 °C samples confirmed the existence of the $Fe_3Nb_7B_8$ compound very likely present in the raw metallic glass, as already said, and showed the presence of the FeB, and Fe_2B phases and of a Fe solid solution. At 805°C, an additional phase is formed, namely $BFe_{14}Y_2$. At 850°C, no significant evolution is noticed. The X-ray diffractogram of the remelt and fully crystallized sample heated up to 1400°C agrees with this phases identification. It verifies the existence of the five phases already detected by EPMA (figure 13), namely a Fe terminal solid solution [phase a], $Fe_3Nb_7B_8$ [phase b], FeB and Fe_2B [phase c] and $BFe_{14}Y_2$ [phase e].

In addition, the presence of a eutectic constituent comprising Fe [phase a] and Fe_2B [phase c] (figure 12) is consistent with the Fe-B equilibrium phase diagram which indicates a eutectic transformation at 1177°C **[13]**. This equilibrium temperature is nevertheless curiously a few degrees higher than the 1106°C onset melting temperature in the DSC signal (figure 4 and table 2).

Finally, according to the current analyses, Al does not take part significantly to the different steps of crystallization.

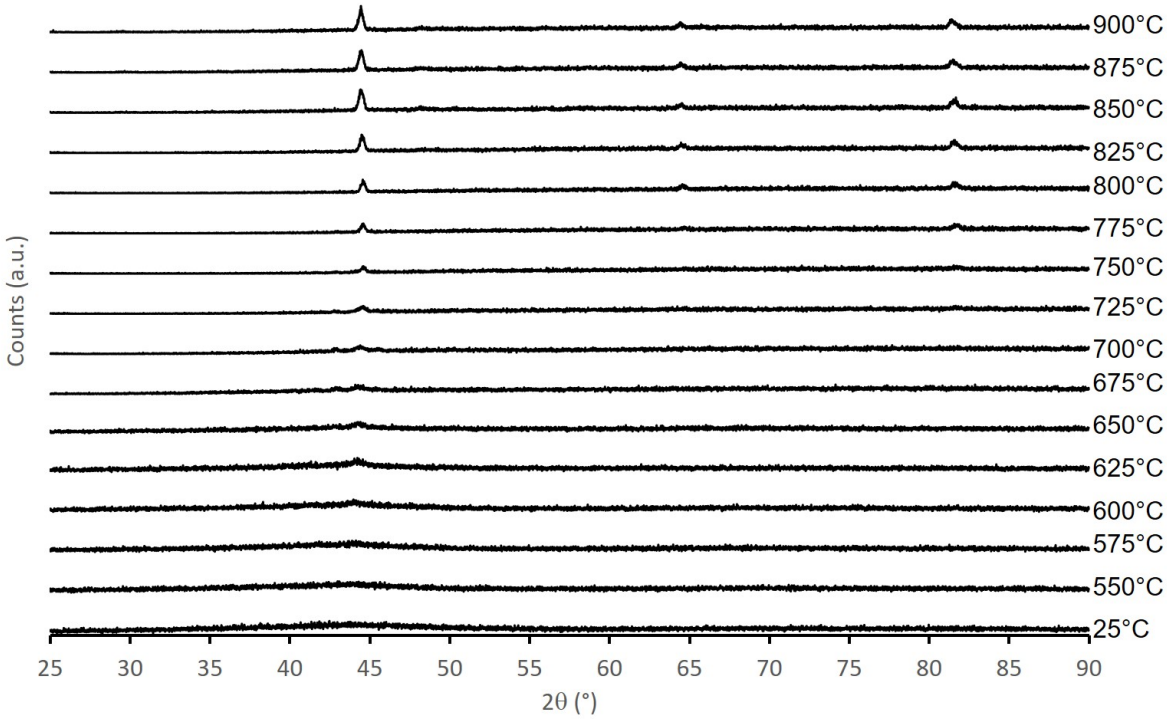

Figure 14: In-situ X-ray diffraction patterns of the ribbon *vs.* temperature.

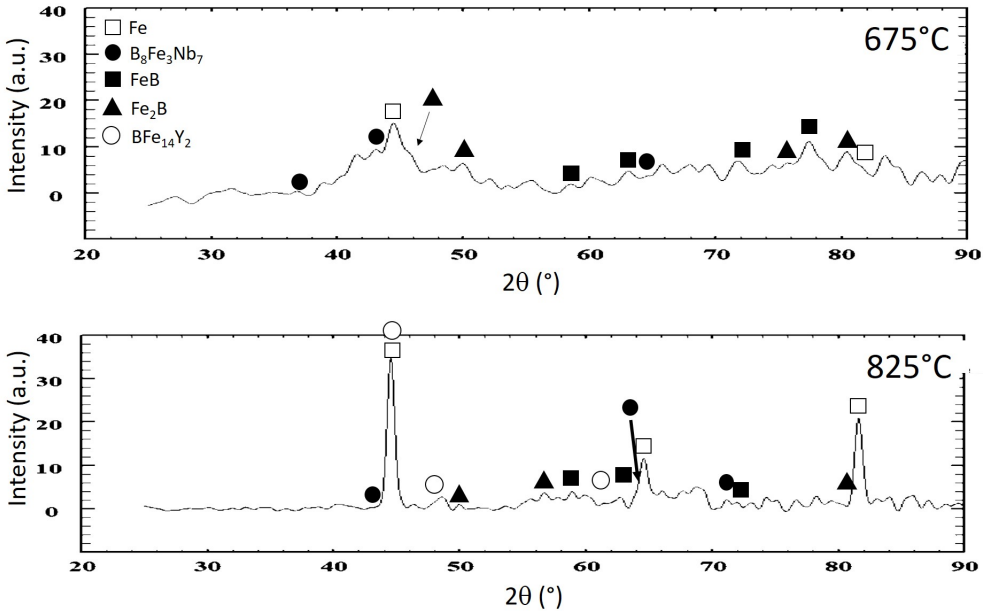

Figure 15: X-ray diffraction pattern of the ribbon continuously heated at 10 K/min up to 675°C and up to 825°C.

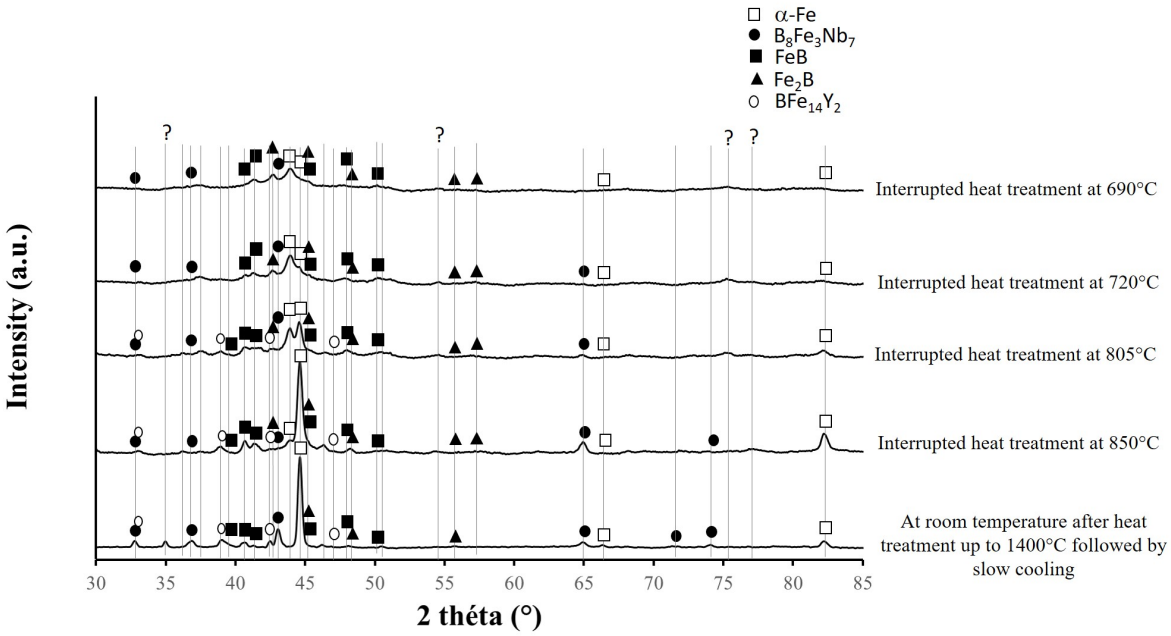

Figure 16: Room temperature X-ray diffractograms of the bulk metallic glass heated at 10 K/min up to a 690°C, 720°C, 805°C, 850°C or 1400 °C peak temperature. Except the last one, all these samples were cooled at 50 K/min.

3.4. Instrumented hardness

Above all, given the 50 µm thickness of the ribbon, no hardness measurement has been performed on the ribbon because of the low reliability of the measurements on thin samples due to the mounting resin elasticity **[~~26~~28]**.

With regard to the different samples, the loading and unloading curves in figure 17 enable to classify them in two categories according to their behavior: the first class comprises the raw metallic glass and the samples treated at 690, 720, 805 and 850°C, while the second category is limited to the only sample fully crystallized after the 1400°C heat treatment. The second category is more deformable and less hard.

As expected, the bulk metallic glass presents an elastic behavior. Its 500 g Vickers hardness ($HV_{0.5}$), rigidity (S) and reduced Young modulus (E) are 1198±21, 3.95±0.13 N/µm and 174±5 GPa, respectively (tableau 4). Therefore, according to the relationship between the Young Modulus (E) and the fracture strength at an elastic strain of 0.02 (σ_f) reported in the literature ($E \approx 50 \times \sigma_f$) **[1]**, the fracture strength at an elastic strain of 0.02 of the metallic glass should be close to 3480 MPa. The Fe based bulk MG of the metal-metalloid kind are indeed known to be intrinsically brittle because of their covalent bonds between metal-metalloid atomic pairs **[1]**.

Table 4 further shows that:

(i) The mean Young modulus of the metallic glass is similar in all the samples except after a heat treatment at 850°C where it increased a little.

(ii) The average hardness of the bulk sample increases with the interrupted heat treatment peak temperature to reach 1318 $HV_{0.5}$ after an interrupted heat treatment at 850°C. It is on the contrary noticeably reduced to 461 $HV_{0.5}$ after the 1400°C remelting and full crystallization. It is worth noting more or less scattered values of hardness according to the sample (table 4). The more scattered values very likely result from the heterogeneousness of the local microstructure.

Examples of hardness indents are displayed in figure 18. The samples which were given the 690°C, 720°C and 805°C interrupted heat treatments, exhibit some radial cracks propagating from the indent apexes along the indent diagonals axes. Such a feature is characteristic of a brittle material. The ratio of the crack length (l), i.e. the distance between the tip of the indentation and the tip of the crack, and the half diagonal of the indentation (a) is lower than 2.5 which suggests that the cracks are Palmqvist type cracks according to Niihara **[~~27~~29]**. K_{1c} can be estimated by the following equation 4 **[~~28~~30]**:

$$K_{1c} = 0.0143 \times (E/H)^{2/3} \times (l/a)^{-0.5} \times P \times c^{-3/2} \quad (4)$$

with c the distance between the indentation centre and the tip of the crack, E the Young modulus (in GPa), H the hardness (in GPa) measured at the P load (in MN), a, c and l in m.
The application of equation 4 to the 690, 720 and 805°C heated samples gives K_{1c} values of 2.0, 3.4 and 3.6 MPa.m$^{0.5}$, respectively. Such estimates are characteristic of brittle materials. They are of the same order of magnitude as those of some Fe based metallic glasses **[2]**.

Figure 18 further shows that the indentation shape changes with the heat treatment. Its obvious pincushion morphology with the sample heated up to 850°C arises from a noticeable sinking in, and then plastic deformation of the material around the flat faces of the pyramidal indenter. Such a behavior contrasts with the brittleness of the samples heated up to the lower peak temperatures. The remelt sample is characterized by a significant plastic expulsion of material at the specimen surface at the indentation periphery.

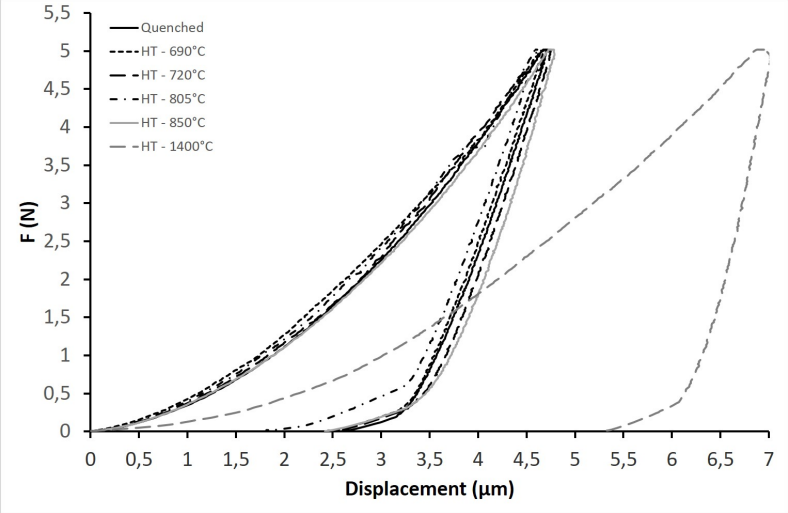

Figure 17: Example of charge-discharge curves of the bulk material either quenched state or after the interrupted heat treatments (HT).

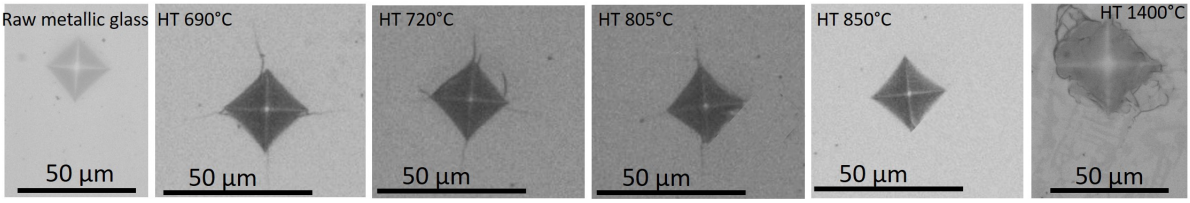

Figure 18: Aspect of the hardness indentations under a 500 g load on the bulk sample at the raw state or after the interrupted heat treatments.

Table 4: Microhardness analysis of the bulk samples heat treated or not.

Sample	Quenched	After interrupted heat treatment at 690°C + cooling	After interrupted heat treatment at 720°C + cooling	After interrupted heat treatment at 805°C + cooling	After interrupted heat treatment at 850°C + cooling	After heat treatment at 1400°C + slow cooling
$HV_{0.5}$	1198±21	1227±106	1189±137	1319±25	1318±35	461±65
E (GPa)	174±5	174±6	178±6	174±3	208±4	172±6
S (N/µm)	3.95±0.13	3.91±0.07	4.06±0.13	3.76±0.06	4.51±0.13	6.32±0.63

4. Discussion

4.1. High glass forming ability (GFA) of the $Fe_{64}B_{24}Y_4Nb_6$ metallic glass

According to the 'confusion principle' proposed by Geer, the glass forming ability, which is the capability of an alloy to form a glassy state **[1]**, tends to increase with the constituent number in the metallic glass since numerous constituents will delay the formation of competing crystalline phases during cooling **[2]**. The GFA is determined by both structural factors (geometrical arrangement of atoms, chemical interactions between atoms, and atomic size effect) and kinetical parameter (cooling rate linked to crystallization kinetics) **[1]**.

Numerous and miscellaneous empirical considerations tend to agree, alone or in combination, with ~~the~~a high GFA of the studied $Fe_{64}B_{24}Y_4Nb_6$ MG:

(i) The large extent of the supercooled liquid region ΔT, defined as Tx_1-Tg (table 2), implies the high stability of the supercooled liquid against crystallization, equivalent to a high GFA. The respective ~~82~~93 or 95°C ΔT ranges for the ribbon and the bulk (table 2) are indeed pretty larger than the usual supercooled liquid region ~~which exists over 40°C in Co, 50°C in Cu, 80°C in La, 63°C in Mg, 45°C in Nd, 65°C in Ni, 94°C in Pd, 75°C in Pr bearing~~ observed in most of the metallic glasses **[2,6,~~29-43~~31-45]**. By way of contrast, the 146°C, 123°C and 125°C extents of ΔT in the $Zr_{42.63}Ti_{12.37}Cu_{11.25}Ni_{10}Be_{23.75}$ **[4]**, $Ti_{41}Zr_{25}Be_{28}Fe_6$ **[4446]** and $Nd_{60}Al_{10}Cu_{10}Fe_{20}$ **[4]** amorphous alloys respectively are larger than the present ones.

(ii) According to the Turnbull criteria based on the relationship between the kinetics of crystals nucleation and the melt viscosity, the reduced glass transition temperatures (Tg/T melting) of 0.6 for the ribbon and the bulk metallic glass (table 2) are very close to 2/3, which means a very sluggish crystallization and thus a high GFA **[1,4]**.

(iii) It is also well-known that deep eutectics alloy compositions are good glass formers **[1]**. It is very likely the case of the present alloy whose composition does not differ markedly from that of the Fe-17at% B and Fe-Nb deep eutectics **[13]**.

~~(iv) The fragility index m **[2425]** remains under 16 which means that the glass is a strong liquid with a high glass forming ability (table 3).~~

(iv) Egami and Miracle have suggested that important lattice strains due to the addition of chemical elements to Fe can lead to a glassy state. The induced deformation disturbs the Fe crystal lattice which becomes amorphous once a critical strain is exceeded **[1]**. ~~The solute atoms of B, Nb and Y very likely occupy some interstitial and/or substitutional positions in the host lattice of Fe.~~ The large differences of atomic radii between Fe and B, Y or Nb, namely -31

pm, 19 pm and 53 pm, respectively are sufficient to generate important local strain at the lattice scale because of contraction or dilatation of the Fe lattice.

(v) The high GFA of the studied metallic glass may also be consistent with the larger electronegativity of the major addition element compared to Fe **[2]**: it is indeed 2.04 for B against 1.83 for Fe.

(vi) ~~According to Shen, the Fe based bulk MGs with a high GFA should satisfy the following empirical rules : the alloy must have at least 3 components, the alloy must contain 2 or more metallic elements with different atomic sizes and near-zero heats of mixing, the metallic elements must have large negative heats of mixing with the metalloids, the total metalloid content must be in the vicinity of 20 at.%, crystalline nucleants such as oxide inclusions must be carefully removed by dissolving the oxides in a flux, or by neutralizing the oxygen by dissolving it in the melt **[1,4546]**.~~ The stoichiometry of the current alloy checks the empirical rules developed by Shen **[1,47]** for the case of Fe based bulk MGs with a high GFA. Fe, Nb and Y are metallic elements with different atomic sizes; and B is a metalloid whose content is 24 at.%, and thus in the vicinity of 20 at%. In addition, the Y-B, Fe-B, Nb-B, Fe-Y and Fe-Nb heats of mixing amount to -50 to -35 kJ/mol, -26 to -16 kJ/mol, -39 kJ/mol, -1 kJ/mol and -23 kJ/mol, respectively **[8,11,12,14]**, which means that the cohesive forces between these atoms are strong. These large negative heats of mixing caused a confusion effect in the present system of 4 elements with different atomic radii. The ensuing dense atomic packing in the liquid state inhibits crystallization and then promotes glass formation during the solidification **[8]**. Atomic simulations, EXAFS and XRD **[~~46~~48]** also proved the existence of local composition fluctuations in the metallic glasses, which can affect the nucleation and growth of competing crystalline phases during solidification. Some Nb and Y segregations may exist in the metallic glass as shown by **[~~46~~48]**. The presence of large-sized Nb and Y atoms (181 and 147 pm, respectively), with an atomic size difference of at least 12% with Fe and B verifies the empirical rules suggested by Inoue, Egami and Miracle for improving the GFA, as they contribute to the disorder in the metallic glass and frustrate the atom arrangement of the competing crystalline phases.

~~The high GFA of the current alloys is consistent with the~~ The aforementioned criteria and *a fortiori* ~~with~~ their combination tend to suggest that the current alloys present a high GFA.

Other factors, not obvious at this early stage of the present investigation, may also contribute to the high GFA of the present alloy. They concern the formation of both (i) icosahedron like clusters, which are incompatible with traditional crystalline phases and which increase the dynamic barrier for atomic mobility when they connect to form networks and (ii) Y-centered large polyhedrons in Y and Nb-containing alloys **[~~46~~48]**.

Dealing with the literature data, the Fe-based metallic glasses with B rich compositions have already been shown to present wide supercooled liquid regions **[2,~~47~~49]** and small additions of Nb and/or Y were evidenced to significantly promote the GFA of Fe-B alloys **[1,2,5,7,8,12,15,~~48~~50]**. In Fe-Nb-B alloy, an addition of Y, which is characterized by the lowest atomic mobility among the 4 elements **[9]**, was reported to improve the thermal stability of the glassy phase by leading to a network of densely packed Fe-Nb-B skeletons in which trigonal prisms are connected with each other in an edge sharing mode through multi-bonding atoms of lanthanide and transition metal **[2,12]**. The presence of Y in the Fe-based bulk metallic glass further led to the suppression of heterogeneous nucleation in bulk $Fe_{74}B_{17}Y_3Nb_6$ metallic glass **[12]** while Nb (compared to Ti, Al, Hf or Zr) was evidenced to broaden the supercooled region in a $(Y_{0.06}Fe_{0.72}B_{0.22})_{98}Nb_2$ metallic glass **[2,~~49~~51]**.

4.2. Second inflection event in the supercooled liquid region

The presence of a second inflection in the DSC curve (figures 4 and 5) which corresponds to an exothermic event in the supercooled liquid region is very likely due to a chemical short-range ordering that is a local atomic structure reordering **[10,11]** caused i) by the positive mixing enthalpy between Y and Nb of 30 kJ/mol **[2,15]** - these elements indeed present a repulsive interaction – and ii) by the strong affinity between B and Fe, Y and Nb compatible with their large heats of mixing, which leads to the formation of random dense packing structure keeping the undercooled liquid more stable **[2]**. This observation was already made in metallic glasses with a similar stoichiometry namely $Fe_{68.76}B_{22.92}Y_{4.5}Nb_{3.82}$ **[15]** and Fe_{72-x} $B_{22}Y_6Nb_x$ (x=0 – 6 at.%) **[11]**. Local atomic ordering during heat treatments before crystallization was detected by Y K-edge extended X-ray absorption fine structure (EXAFS) measurements in a metallic glass with a similar composition as the current one **[11]**.

4.3. Glass transition and primary crystallization activation energies

The glass transition activation energy corresponds to the energy required by a group of atoms to jump from one metastable state where the atoms are almost static and the alloy is brittle, to another state where the atoms vibrations increase and the alloy presents a rubber-like material flow. Around Tg, the structure of the system relaxes and the atoms begin to rearrange. The activation energy of primary crystallization is the amount of energy necessary for the nucleation of the first crystalline phase.

The apparent activation energies for the current metallic glass estimated by both the Kissinger's and the Moynihan's methods are very close to each other whatever the glass transition or the primary crystallization case (table 3). The activation energy for glass transition was found to be lower than that of primary crystallization, which means that the crystallization rate is lower than the glass transition rate. The low value of the apparent activation energy of the glass transition has perhaps to do with an important free volume induced by the formation of organized domains in the quenched ribbon (figure 2).

The rigorous comparison of the current apparent activation energies with the literature is however not possible because of the lack of data for quaternary metallic glasses with a similar composition. Anyway, the comparison would have been ticklish since it depends not only on the chemical composition of the metallic glass but also on the efficiency of quenching which governs the structure compactness as well as the atoms arrangement in the glassy phase.

With regard to the methods used to determine the activation energies, the Kissinger's approach assumes that the transformed fraction at the peak temperature ~~or at the onset temperature of reaction~~ does not depend on the heating rate **[22]**. However, the latter hypothesis is not necessary justified since the free volume variation in the not transformed and solute rich material may modify the frequency parameter in the rate constant of the Arrhenius equation which intervenes in the Kissinger's equation. Thus the transformed fraction at the peak ~~or onset~~ temperature can change with the heating rate. The Kissinger's method has also been criticized by Khonik *et al.* since it leads to apparent attempt frequencies for glass transition and primary crystallization that are too high by many orders of magnitude compared to the Debye frequency (10^{13} s^{-1}). According to the same authors, the apparent atoms frequencies should be at most higher than the Debye frequency by one or two orders of magnitude owing to the atoms vibration [**~~50~~52**]. Nevertheless, the atoms at the glassy state or in the supercooled liquid state are not linked to their neighbors in the same manner as in a crystal, which could explain the difference obtained with regard to the frequency.

In addition, the conditions necessary to the validity of the Moyhinan's method are: (i) the structural relaxation is describable by a temperature-independent distribution of relaxation times and (ii) the glass is cooled from a temperature well above the transition region and

subsequently reheated at the same rate from a starting temperature well below the transition region [~~23~~24]. Once again, both conditions are not strictly verified by number of studies and more particularly the first one which depends on the atoms arrangement at the quenched state.

4.4. Crystallization of the metallic glass

According to the analyses of the present alloy in the fully crystallized state, various phases have been identified, that is a Fe solid solution, FeB, Fe_2B, $Fe_3Nb_7B_8$ and $BFe_{14}Y_2$ (figures 8, 10, 15 and 16). The formation of Fe_2B and FeB is consistent with their -67.4 kJ/mol and -65.8 kJ/mol low energy of formation at 727°C, respectively **[13]**. The formation of an Fe terminal solid solution, and of the FeB and Fe_2B compounds can also be explained by the high Fe and B contents in the alloy.

The Fe solid solution and the Fe_2B have also been identified in
i) ternary metallic glasses such as

a) $Fe_{90-x}Nb_{10}B_x$ (with x=10, 20 or 30), which also contains Fe_3B [~~51~~53]. When *x* is equal to 20 or 30, these phases have originated from the decomposition of the $(Fe,Nb)_{23}B_6$ primary crystal and when x=10, they were formed by the transformation of a metastable supersaturated α-Fe solid solution.
b) $Fe_{70}Nb_{10}B_{20}$ together with FeNbB and $Fe_{33}Nb_5B_{10}$ [~~52~~54].
c) $Fe_{71.2}Nb_{6.1}B_{22.7}$ (thin film) after annealing at 610°C for 10 min [~~53~~55].
d) $Fe_{62}Nb_8B_{30}$, together with $FeNb_2B_2$ [~~54~~56].

ii) quaternary alloys similar to the current one, namely $Fe_{70.56}B_{21.56}Y_{5.88}Nb_2$ (4 mm diameter rod) and the $Fe_{72}B_{22}Y_4Nb_2$ (5 mm diameter rod) together with NbB and Fe_3B [~~49~~51], while the crystallization of $Fe_{74}B_{17}Y_3Nb_6$ led to the formation of an α-Fe solid solution **[12]**.

The $Fe_3Nb_7B_8$ compound has on the contrary never been identified in metallic glasses with a similar composition. This boride, whose structure reminds the clusters one presented by **[9]**, has been put into evidence for the first time in the bulk form by Zheng et al. **[16]**. These authors have synthesized $Fe_3Nb_7B_8$ by arc-melting followed by annealing at 1000°C for 12 h and at 1500°C for 48 h. This suggests that, in the current study, this phase, which is essentially antiferromagnetic below T_N = 240 K **[16]**, was very likely already present at the quenched sate of the initial ribbon. This phase is known to decompose into NbB, Fe_2B and α-Fe at 1580°C via an endothermal transformation **[16]**.

The $BFe_{14}Y_2$ compound was not identified in similar specimens in the literature, instead, some authors have reported the formation of $B_{14}Fe_{62}Y_3$ in Fe-B-Y system [~~55~~57].

It is worth noting that the $Fe_{23}B_6$ boride was not detected in the current samples. A very likely explanation consists in its decomposition at higher temperature like in a previous work [~~51~~53]. $Fe_{23}B_6$ was indeed reported to form together with α-Fe in Fe-B-Y systems [~~46,56,57~~48,58,59] and to be the primary precipitate in Fe-B-Nb rich systems [1,~~47~~49] such as $Fe_{68.76}B_{22.92}Y_{4.5}Nb_{3.82}$ **[15]**, and the $Fe_{80}Nb_{10}B_{10}$, $Fe_{70}B_{20}Nb_{10}$ and $Fe_{60}B_{30}Nb_{10}$ alloys according to ab initio molecular dynamical simulation [~~47~~49]. The large $Fe_{23}B_6$ fcc cell phase with a 1.1 nm lattice parameter and a unit volume consisting of 96 atoms **[4]** can host Y atoms on its 8c sites up to a 6.9 at.% Y content. Such a concentration entails a serious distortion of the $Fe_{23}B_6$ crystal lattice hence the so-called Y-induced geometry frustration **[1]**. This phase presents a local anti-Archimedean atomic configuration similar to that of the Fe-Nb-B glassy alloys. Some authors thus explain the primary precipitation of $Fe_{23}B_6$ by the similarity between this phase and the local atomic configurations of the supercooled liquid **[1,15]**. Contrarily, other authors assess that the formation of $Fe_{23}B_6$ is difficult since it requires a long range atomic diffusion compared to α-Fe, which grows from the bcc-like medium range order regions in a $Fe_{84}B_9Nb_7$ glassy alloy **[2]**.

The formation of other phases in the open literature can be explained by the local composition fluctuations in the metallic glasses after solidification **[~~46~~48]** which can affect the nucleation and growth of competing crystalline phases and the nature of the formed phases.

5. Conclusions

- The investigated $Fe_{64}B_{24}Y_4Nb_6$ metallic glass with a high glass forming ability presents a glass transition temperature of 585~~596~~°C and crystallizes from 677°C. Whatever its calculation with the Kissinger's or the Moyhinan's method, the activation energy of the glass transition was lower than that of primary crystallization. The activation energy of the glass transition was low very likely because of the free volume importance.
- X-ray diffractometry and electron diffraction revealed that the primary crystals are FeB and Fe_2B. The XRD analysis and the electron probe microanalyses of the fully crystallized alloy put into evidence the additional presence of an Fe solid solution and of the $Fe_3Nb_7B_8$ and $BFe_{14}Y_2$ compounds.
- The hardness, the Young modulus and the rigidity of the bulk metallic glass are 1198±21 $HV_{0.5}$, 174±5 GPa, 3.95±0.13 N/µm respectively vs. 461±65 $HV_{0.5}$, 172±6 GPa and 6.32±0.63 N/µm for the fully crystallized alloy. Instrumented hardness is also suitable to characterize the effect of partial or full crystallization on the alloy ductility.

Aknowledgments

The authors are very thankful to Séverine Bellayer, ENSCL, France for the electron probe microanalyses, to David Troadec, IEMN, France for the thin foils cutting by FIB, to Pascal Roussel, UCCS, Lille University, France for the in-situ XRD analyses and to Damien Creton, UMET, Lille University, France for the instrumented microhardness tests. The TEM facility in Lille (France) is supported by the Conseil Régional du Nord-Pas de Calais, and the European Regional Development Fund (ERDF). The authors also thank the Chevreul Institute (FR 2638) for its help in the development of this work. Chevreul Institute is supported by the « Ministère de l'Enseignement Supérieur et de la Recherche », the « Région Nord-Pas de calais » and the « Fonds Européen de Développement des Régions ».

References

[1] C. Suryanarayana, A. Inoue, Iron-based bulk metallic glasses, Intern. Mater. Rev. 5(3) (2013) 131-166

[2] H.X. Li, Z.C. Lu, S.L. Wang, Y. Wu, Z.P. Lu, Fe-based bulk metallic glasses: Glass formation, fabrication, properties and applications, Prog. Mater. Sci. 103 (2019) 235-318

[3] A. Inoue, Stabilization of metallic supercooled liquid and bulk amorphous alloys, Acta Mater. 48 (2000) 279-306

[4] W.H. Wang, C. Dong, C.H. Shek, Bulk metallic glasses, Mater. Sci. Eng. R44 (2004) 45-89

[5] C.Y. Lin, H.Y. Tien, T.S. Chin, Soft magnetic ternary iron-boron based bulk metallic glasses, Appl. Phys. Letters 86 (2005) 162501

[6] Y. Zhao, P.F. Liu, L. Wu, B. Zhang, K. Sato, The role of open spaces to glass-forming ability in bulk metallic glasses, Intermetallics 100 (2018) 112-115

[7] D.H. Kim, J.M. Park, D.H. Kim, Development of quaternary Fe-B-Y-Nb bulk glassy alloys with high glass-forming ability, J. Mater. Res. 22 (2007) 471-477

[8] X.M. Huang, C.T. Chang, Z.Y. Chang, X.D. Wang, Q.P. Cao, B.L. Shen, A. Inoue, J.Z. Jiang, Formation of bulk metallic glasses in the Fe-M-Y-B (M=transition metal) system, J. All. Cmpnds. 460 (2008) 708-713

[9] J. Ge, H. He, J. Zhou, C. Lu, W. Dong, S. Liu, S. Lan, Z. Wu, A. Wang, L. Wang, C. Yu, B. Shen, X. Wang, In-situ scattering study of liquid-liquid phase transition in Fe-B-Nb-Y supercooled liquids and its correlation with glass-forming ability, J. All. Cmpnds. 787 (2019) 831-839

[10] S. Lee, H. Kato, T. Kubota, A. Makino, A. Inoue, Fabrication and soft-magnetic properties of Fe-B-Nb-Y glassy powder compacts by spark plasma sintering technique, Intermetallics 17 (2009) 218-221

[11] X.M. Huang, X.D. Wang, Y. He, Q.P. Cao, J.Z. Jiang, Are there two glass transitions in Fe-M-Y-B (M=Mo, W, Nb) bulk metallic glasses? Scripta Mater. 60 (2009) 152-155

[12] D.S. Song, J.H. Kim, E. Fleury, W.T. Kim, D.H. Kim, Synthesis of ferromagnetic Fe-based bulk glassy alloys in the Fe-Nb-B-Y system, J. All. Cmpnds. 389 (2005) 159-164

[13] Smithells Metal Reference Book, 7th ed., E.A. Brandes and G.B. Brook, eds., Oxford, U.K., 1992.

[14] I. Kaban, P. Jovari, A. Waske, M. stoica, J. Bednarcik, B. Beuneu, N. Mattern, J. Eckert, Atomic structure and magnetic properties of Fe-Nb-B metallic glasses, J. All. Cmpnds. 586 (2014) S189-S193

[15] S. Lee, H. Kato, T. Kubota, K. Yubuta, A. Makino, A. Inoue, Excellent thermal stability and bulk glass forming ability of Fe-B-Nb-Y soft magnetic metallic glass, Mater. Trans. 49(3) (2008) 506-512

[16] Q. Zheng, R. Gumeniuk, H. Borrmann, W. Schnelle, A.A. Tsirlin, H. Rosner, U. Burkhardt, M. Reissner, Y. Grin, A. Leithe-Jasper, Ternary borides $Nb_7Fe_3B_8$ and $Ta_7Fe_3B_8$ with Kagome-type iron framework, Dalton Transactions 45(23) (2016) 9590-9600

[17] P. Rizzi, C. Antonione, M. Baricco, et al. Crystals and nanocrystals in rapidly solidified Al-Sn alloys. Nanostructured Mater. 10(5) (1998) 767-776

[18] M. Bletry, P. Guyot, Y. Brechet, J.J. Blandin, J.L. Soubeyroux, Homogeneous deformation of bulk metallic glasses in the super-cooled liquid state, Mater. Sci. Eng. A387-389 (2004) 1005-1011

[19] M. Bletry, P. Guyot, Y. Brechet, J.J. Blandin, J.L. Soubeyroux, Homogeneous deformation of Zr-Ti-Al-Cu-N bulk metallic glasses, Intermetallics 12 (2004) 1051-1055

[20] D. Yao, L. Deng, M. Zhang, X. Wang, N. Tang, J. Li, A size-dependent constitutive model of bulk metallic glasses in the supercooled liquid region, Scientific reports, 2015, 5:8083 |DOI:10.1038/srep08083

[21] Z. Shao, M. Gopinadhan, G. Kumar, S. Mukherjee, Y. Liu, C.S. O'Hern, J. Schroers, C.O. Osuji, Size-dependant viscosity in the super cooled liquid state of a bulk metallic glass, Appl. Phys. Letters 102, 221901 (2013), doi: 10.1063/1.4808342

[22] H.E. Kissinger, Reaction kinetics in differential thermal analysis, Anal. Chem. 29(11) (1957) 1702-1706

[23] H.E. Kissinger, Variation of peak temperature with heating rate in differential thermal analysis, J. Res. Nat. Bureau of Satndards 57(4) (1956) 217-221

[~~23~~24] C.T. Moynihan, A.J. Easteal, J. Wilder, J. Tucker, Dependance of glass transition temperature on heating and cooling rate. J. Phys. Chem. 78(26) ~~(2008)~~ (1974) 2673-2677 DOI: 10.1021/j100619a008

[~~24~~25] A.T. Patel, A. Pratap, Study of glass transition kinetics for Co66Si12B16Fe4Mo2 metallic glass, Int. J. Mod. Phys.: Conf. Series 22 (2013) 321-326

[~~25~~26] R. Böhmer, Non-linearity and non-exponentiality of primary relaxations, J. Non Cryst. Solids 172-174 (1994) 628-634

[~~25~~27] Crystals files PDF72-1301 Fe_2B and PDF-751065 FeB

[~~26~~28] G.A. Crawford, N. Chawla, M. Koopman, K. Carlisle, K.C. Krishan, Effect of mounting material compliance on nanoindentation response of metallic materials, Adv. Eng. Mater. 11(1-2) (2009) 45-51

[~~27~~29] K. Niihara, R. Morena, D.P.H. Hasselman, in Fracture Mechanics of Ceramics, eds R.C. Bradt, A.G. Evans, P.P. Hasselman, F.F. Lange, Plenum Press, New York, 5 (1983) 97-105

[~~28~~30] M.T. Laugier, New Formula for indentation toughness in ceramics, Journal of Mater. Sci. Letters 6 (1987) 355-356

[~~29~~31] Z. Wang, J. Tan, B.A. Sun, S. Scudino, K.G. Prashanth, W.W. Zhang, Y.Y. Li, J. Eckert, Fabrication and mechanical properties of Al-based metal matrix composites reinforced with Mg65Cu20Zn5Y10 metallic glass particles, Mater. Sci. Eng. A 600 (2014) 53-58

[~~30~~32] H. Men, Z.Q. Hu, J. Xu, Bulk metallic glass formation in the Mg-Cu-Zn-Y system, Scripta Mater. 46 (2002) 399-703

[~~31~~33] J.Y. Kim, S. Scudino, U. Kühn, B.S. Kim, M.H. Lee, J. Eckert, Production and characterization of brass-matrix composites reinforced with $Ni_{59}Zr_{20}Ti_{16}Si_2Sn_3$ glassy particles, Metals 2 (2012) 79-94

[3234] J. Subramanian, S. Seetharaman, M. Gupta, Processing and Properties of aluminum and magnesium based composites containing amorphous reinforcements: a review, Metals 5 (2015) 743-762

[3335] H. Fujii, Y. Sun, K. Inada, Y. Ji, Y. Yokoyama, H. Kimura, A. Inoue, Fabrication of Fe-based metallic glass particle reinforced Al-based composite materials by friction stir processing, Mater. Trans. 52(8) (2011) 1634-1640

[3436] Z. Jamili-Shirvan, M. Hadad-Sabzevar, J. Vahdati-Khaki, N. Chen, Q. Shi, K.-F. Yao, Microstructure characterization and mechanical properties of Ti-based bulk metallic glass joints prepared with friction stir spot welding process, Mater. Design 100 (2016) 120-131

[3537] J. Gao, J. Sharp, D. Guan, W.M. Rainforth, I. Todd, New compositional design for creating tough metallic glass composites with excellent work hardening, Acta Mater. 86 (2015) 208-215

[3638] S. Lin, D. Liu, Z. Zhu, D. Li, H. Fu, Y. Zhuang, H. Zhang, H. Li, A. Wang, H. Zhang, New Ti-based bulk metallic glasses with exceptional glass forming ability, J. Non-Cryst. Solids 502 (2018) 71-75

[3739] A. Kuball, O. Gross, B. Bochtler, B. Adam, L. Ruschel, M. Zamanzade, R. Busch, Development and characterization of titanium-based bulk metallic glasses, J. All. Cmpnds. 790 (2019) 337-346

[3840] X. Ma, Q. Li, L. Chang, C. Chang, H. Li, Y. Sun, Enhancement of GFA and mechanical properties of Ni-based numk metallic glasses through Fe addition, Intermetallics 90 (2017) 58-62

[3941] M.L. Tokarz, S.A. Speakman, W.D. Porter, J.C. Bilello, Stability of Ni-based bulk metallic glasses, J. Non-Crystall. Solids 352 (2006) 3236-3243

[4042] Z. Zhou, Q. Wei, Q. Li, B. Jiang, Y. Chen, Y. Sun, Development of Co-based bulk metallic glasses as potential biomaterials, Mater. Sci. Eng. C 69 (2016) 46-51

[4143] G. Zhang, H. Zhang, S. Yue, R. Cheng, A. Wang, A. He, Y. Dong, H. Ni, C.6T. Liu, Preparation of non-magnetic and ductile Co-based bulk metallic glasses with high GFA and hardness, Intermetallics 107 (2019) 47-52

[4244] F. Hu, Q. Luo, B. Shen, Thermal, magnetic and magnetocaloric properties of FeErNbB metallic glasses with high glass-forming ability, J. Non-Cryst. Solids 512 (2019) 184-188

[4345] X. Hui, W. Dong, G.L. Chen, K.F. Yao, Formation, microstructure and properties of long-period Mg-based bulk metallic glass composites, Acta Mater. 55 (2007) 907-920

[4446] P. Gong, S. Wang, Z. Liu, W. Chen, N. Li, X. Wang, K.F. Yao, Lightweight Ti-based bulk metallic glasses with superior thermoplastic formability, Intermetallics 98 (2018) 54-59

[4547] T.D. Shen, R.B. Schwarz, Bulk ferromagnetic glasses prepared by flux melting and water quenching, Appl. Phys. Letters 75 (1999) 5, https://doi.org/10.1063/1.124273

[4648] Q. Yu, X.D. Wang, H.B. Lou, Q.P. Cao, J.Z. Jiang, Atomic packing in Fe-based metallic glasses, Acta Mater. 102 (2016) 116-124

[4749] C.C. Yuan, C. Deng, H.P. Zhang, M.Z. Li, B.L. Shen, Ab initio simulations of the atomic and electronic environment around B in Fe-Nb-B metallic glasses, Intermetallics 112 (2019) 106501

[4850] K. Yoshitomi, Y. Nakama, H. Ohtani, M. Hasebe, Thermodynamic analysis of the Fe-Nb-B ternary system, ISIJ Intern. 48(6) (2008) 835-844

[4951] H.W. Chang, Y.C. Huang, C.W. Chang, C.C. Hsieh, W.C. Chang, Soft magnetic properties and glass formability of Y-Fe-B-M bulk metals (M=Al, Hf, Nb, Ta and Ti), J. All. Cmpnds. 472 (2009) 166-170

[5052] V.A. Khonik, K. Kitagawa, H. Morii, On the determination of the crystallization activation energy of metallic glasses, J. Appl. Phys. 87(12) (2000) 8440-8443

[5153] M. Imafuku, S. Sato, H. Koshiba, E. Matsubara, A. Inoue, Structural variation of Fe-Nb-B metallic glasses during crystallization process, Scripta Mater. 44 (2001) 2369-2372

[5254] T.A. Sviridova, T.R. Chueva, M.V. Gorshenkov, E.V. Shelekhov, N.P. Dyakonova, P.A. Borisova, A new metastable phase in Fe-Nb-B system, J. All. Cmpnds. 658 (2016) 525-532

[5355] J.H. Yao, C. Hostert, D. Music, A. Frisk, M. Björck, J.M. Schneider, Synthesis and mechanical properties of Fe-Nb-B thin film metallic glasses, Scripta Mater. 67 (2012) 181-184

[5456] T. Itoi, A. Inoue, Thermal stability and soft magnetic properties of Fe-Nb-B amorphous alloys with high boron concentrations, Mater. Trans. JIM 40(7) (1999) 643-647

[5557] D.B. de Mooij, J.L.C. Daams, K.H.J. Buschow, A metastable compound in the Y-B-Fe system. Philips J. Res. 42(3) (1987) 339-349

[5658] X.M. Huang, X.D. Wang, J.Z. Jiang, Origin of high glass forming ability of Y containing Fe-B based alloys, J. All. Cmpnds. 485 (2009) L35-L38

[5759] A. Hirata, Y. Hirotsu, K. Amiya, N. Nishiyama, A. Inoue, Fe23B6 type quasicrystal-like structures without icosahedral atomic arrangement in an Fe-based metallic glass, Phys. Rev. B 80 (2009)140201

Figure captions

Figure 1: Room temperature X-ray diffraction patterns of the shiny and dull faces of the ribbon at the quenched state.

Figure 2: TEM image of the quenched alloy ribbon and the corresponding SAEDP

Figure 3: Microstructure within a bulk sample at the raw state (EPMA/BSE).

Figure 4: DSC pattern of the metallic glass at a heating rate of 10 K/min. The sample mass was 6.710 mg for the ribbon (a) and 74.719 mg for the bulk (b) sample, respectively. The inserts in the figure are local enlargements of the curves evidencing the glass transition.

Figure 5: Effect of heating rate on the metallic glass ribbon phase transformations (the samples masses were respectively 6.710, 2.964, 2.730 and 2.801 mg for the 10, 20, 40 and 50°C/min heating rates).

Figure 6: Kissinger analysis for the ribbon by considering the 10 K/min, 20 K/min, 40 K/min and 50 K/min (a) plus the 500, 1000 and 5000 K/s (b) heating rates. The lines are the linear fits for $\ln(\beta/T^2)$ *vs.* 1/RT, where T is either the glass transition peak temperature or the peak temperature ~~at peak maximum~~ of the primary crystallization.
Moynihan's method for the ribbon by considering the 10 K/min, 20 K/min, 40 K/min and 50 K/min (c) plus the 500, 1000 and 5000 K/s (d) heating rates. The lines are the linear fits for $\ln(\beta)$ *vs.* 1/T, where T is ~~either~~ the glass transition temperature at the peak maximum ~~or the maximum peak temperature of the primary crystallization~~.

Figure 7: Microstructure of the ribbon heated up to 681°C with the 10 K/min heating rate (HAADF image).

Figure 8: $Fe_3Nb_7B_8$ crystal structure of zone 1 in figure 7: atomic stacking in the (0001) planes: HAADF (a); schematics of the atomic positions in the present orientation (b); experimental electron diffraction pattern (c) and its simulation (d) along the [0001] zone axis.

Figure 9: Defects in $Fe_3Nb_7B_8$ crystal (zone 1 in figure 7): dislocations and twins (HRTEM) (a) and atomic disorder (HAADF) (b).

Figure 10: 150 nm sized particles (of zone 2 in figure 7) inside the matrix: (a) TEM image and (b) associated selected area electron diffraction pattern.

Figure 11: HAADF and EELS intensity maps of the Fe-$L_{3,2}$ (708 eV), Nb-$M_{5,4}$ (205 eV) and B-K (188 eV), O-K (530 eV) and Y-$L_{3,2}$ (2080 eV) edges for the zones 1, 2 and 3.

Figure 12: BSE/SEM micrograph of the ribbon after the DSC treatment up to 1400°C and associated B Kα, Fe Kα, Nb Kα, Y Kα and O Kα X-ray maps (WDS, EPMA). The color bar indicates the element content in at.%.

Figure 13: BSE/SEM micrograph of the bulk metallic glass after the DSC treatment up to 1400°C and associated B Kα, Fe Kα, Nb Kα, Y Kα and O Kα X-ray maps (WDS, EPMA). The color bar represents the element content in at.%.

Figure 14: In-situ X-ray diffraction patterns of the ribbon *vs.* temperature.

Figure 15: X-ray diffraction pattern of the ribbon continuously heated at 10K/mn up to 675°C and up to 825°C.

Figure 16: Room temperature X-ray diffractograms of bulk metallic glass after interrupted thermal treatment at 690°C, 720°C, 805°C, 850°C, and after heat treatment up to 1400°C and slow cooling.

Figure 17: Example of charge-discharge curves of the raw bulk metallic glass (quenched state) and of the bulk sample after heat treatments (HT).

Figure 18: Aspect of hardness indents under a 500 g load of the bulk sample in raw state and after various heat treatments.